Science Advances
AAAS

advances.sciencemag.org/cgi/content/full/6/24/eaba0606/DC1

Supplementary Materials for

Acoustic streaming vortices enable contactless, digital control of droplets

Peiran Zhang, Chuyi Chen, Xingyu Su, John Mai, Yuyang Gu, Zhenhua Tian, Haodong Zhu, Zhanwei Zhong, Hai Fu, Shujie Yang, Krishnendu Chakrabarty, Tony Jun Huang*

*Corresponding author. Email: tony.huang@duke.edu

Published 10 June 2020, *Sci. Adv.* **6**, eaba0606 (2020)
DOI: 10.1126/sciadv.aba0606

The PDF file includes:

Other Supplementary Material for this manuscript includes the following:

(available at advances.sciencemag.org/cgi/content/full/6/24/eaba0606/DC1)

Table S1. Summary of the operational parameters used in the device shown in Fig. 4F. The parameters can be changed for different applications. Notes: † Splitting of droplets with the transducer array shown in Fig. 4F is not achievable. ‡ This volume range shown is specific to the transducer array in Fig. 4F (i.e., 49.125 MHz). To manipulate droplets beyond the shown volume range, several key design parameters, including the transducer dimension, wavelength, excitation voltage and the thickness of carrier oil layer, need to be updated. § Characterized by co-incubation experiments with 100 μM Rhodamine 6G (R6G).

Parameter	Description
Liquid handling functions	Transportation, Merging, Gating †
Droplet volume range	80 - 550 nL ‡
Actuation speed	0.7 - 3.7 step/sec
Cross-contamination	10^{-7} ~ 8×10^{-5} % diffusion in oil (20 - 55 °C, R6G §)
Working frequency	49.125 MHz
Working voltage	8.8 - 14.8 Vpp
Transducer dimension	1.18×0.87 mm^2, 1.9 mm unit-to-unit distance
Carrier oil	FC-40, 0.89 – 1.14 mm thick
Parallel manipulation	8 droplets per 8 × 8 array area
Biocompatibility	Oxygen-permeable oil used for cell culture, Streaming speed similar to manual vortexing
Surface degradation	None
Surface adsorption	None

Supplementary Note S1: Simulation for low- and high-amplitude acoustic-wave-fluid interaction

In this work, acoustic streaming induced by acoustic leaky wave in the FC-40 oil was used to manipulate droplets floating on oil at different voltages. Numerical simulation was performed to reveal the 3D streaming pattern in the liquid domain and explain the mechanism of droplet trapping. The governing equation of acoustic streaming are the continuity equation and the Navier-Stokes equation:

$$\rho_0 \nabla \cdot \boldsymbol{v}_{dc} = 0 \tag{1}$$

$$\rho_0 (\boldsymbol{v}_{dc} \cdot \nabla)\boldsymbol{v}_{dc} = -\nabla p_{dc} + \mu \nabla^2 \boldsymbol{v}_{dc} + \left(\mu_b + \frac{1}{3}\mu\right)\nabla(\nabla \cdot \boldsymbol{v}_{dc}) + \boldsymbol{F} \tag{2}$$

where ρ_0 is the fluid density, μ_b and μ are the bulk viscosity and shear viscosity, $\boldsymbol{v_{dc}}$ is the steady streaming velocity, and $\boldsymbol{F}$ is the body force term. In this case, $\boldsymbol{F}$ in Eqn. (2) is the acoustic induced body force that generates acoustic streaming. It can be expressed as the spatial gradient of Reynolds' stress (*34*, *35*):

$$F_j = -\rho_0 \sum_{i=1}^{3} \frac{\partial \overline{v_i v_j}}{\partial x_i} \tag{3}$$

in which $\boldsymbol{v}$ is the leaky SAW velocity, and the subscripts *i*, *j*, *k* represent the components of the variable. Since the harmonic leaky SAW displacement $\boldsymbol{u}$ can be approximately expressed by (*34*)

$$u_x = 0 \tag{4a}$$

$$u_y = A_m e^{i\omega t} e^{-ik_L y} e^{-\alpha k_L z} \tag{4b}$$

$$u_z = -i\alpha A_m e^{i\omega t} e^{-ik_L y} e^{-\alpha k_L z} \tag{4c}$$

By taking $v_i = i\omega u_i$ and taking Eqn. (4a) - (4c) into Eqn. (3), the leaky SAW-induced body force can be expressed as (*35*)

$$F_x = 0 \tag{5a}$$

$$F_y = -(1 + \alpha_1^2) A_m^2 \omega^2 k_i e^{[2(k_i y + \alpha_1 k_i z)]} \tag{5b}$$

$$F_z = -(1 + \alpha_1^2) A_m^2 \omega^2 k_i \alpha_1 e^{[2(k_i y + \alpha_1 k_i z)]} \tag{5c}$$

where $\alpha = i\alpha_1$.

The acoustic streaming pattern in a 3 × 3 × 1.04 mm^3 domain was simulated by solving Eqn. (1) and (2) using Comsol Multiphysics 5.3 (the COMSOL group) with a "Laminar Flow" physics and a "Stationary" solver. The body force (Eqn. (5a)-(5c)) was applied to the wave propagation area with a "volume force" condition. The boundary conditions were set to "symmetry", "slip" and "outlet" at the x = 0 and y = 0 interfaces, the z = 1.04 mm interface, and the x = 3 mm and y = 3 mm interfaces, respectively (according to the axis definition in Fig. S1).

Supplementary Note S2: Dual-mode acoustic streaming

In our work, we observed different acoustic streaming modes with various acoustic power, with which *x*-mode and *y*-mode manipulation scenario can be excited as desired. Here we performed further analysis to better characterize the effect and explore the reason of these two modes. In fact, the acoustic streaming can be classified based on different criteria. One classification of streaming is so-called "slow streaming" and "fast streaming" to assess the impact on the efficiency of acoustofluidic devices (*37*). A dimensionless number called "nonlinear Reynolds number" ($Re_{nl} = \frac{M^2}{Sh^2}$, where M is the acoustic Mach number, and Sh is the shear number defined as $\frac{\delta_v}{L}$, where δ_v is the boundary layer thickness, and L is the characterize length) defined by Menguy and Gilbert (*39*) is used to evaluate and differentiate these two streaming with respect to viscous effects. With this definition, the "slow streaming" has a nonlinear Reynolds number of $Re_{nl} \ll 1$, and on contrary $Re_{nl} > 1$ is defined to be "fast streaming". Furthermore, as indicated in previous studies, researchers observed a flow reversal when $Re_{nl} > 1$, which implies high-amplitude acoustic waves (*40*, *41*).

Supplementary Note S3: Fluidic behaviors at high non-linear Reynolds numbers

Interesting phenomena were observed when the nonlinear Reynolds number Re_{nl} exceeds 1 (i.e., excitation voltage ~ 100 Vpp), specifically for the experimental configuration used in the paper. The fluidic behaviors of FC-40 oil at extremely high amplitude excitations are shown Fig. S6. Generally, the fluidic behavior gradually switches from surface deformation (20 Vpp, i.e., *y*-mode streaming), to jetting mode 1 (40 Vpp, 60 Vpp, 80 Vpp), and to jetting mode 2 (100 Vpp, 130 Vpp). For excitation voltages ranging from 40 Vpp to 80 Vpp, a vertical oil column jetting from the oil-air interface can be observed. This is probably due to the merging of two symmetric fluid jets over the IDT (Rayleigh angle: $\arcsin^{-1}(c_{FC\text{-}40} / c_{water}) = 9^{\circ}$). In this scenario, the horizontal velocity components of the two fluid jets cancel each other out, leading to a larger jet moving up vertically (indicated by the blue arrows). Interestingly, as the excitation voltage increases over a threshold within 80 Vpp – 100 Vpp (i.e., V_T', red shading, Fig. S7B), the fluidic behavior switches from "Jetting mode 1" to "Jetting mode 2". Specifically, the vertical jet in "Jetting mode 1" splits into two symmetric jets following the horizontal

SAW propagation direction as indicated by the red arrows. The acoustic pressures at high excitation amplitudes (e.g., 60 Vpp) is beyond the safe range of common hydrophones, which prevents us from experimentally measuring the nonlinear Reynolds number $\mathrm{Re_{nl}}$ at high amplitude excitations (e.g., $Re_{nl} > 1$). However, the acoustic pressure at high-amplitude excitations can be reasonably predicted. In our previous simulations, a linear relationship between the excitation voltage and the amplitude of surface acoustic waves (SAWs) on the Y-128° LiNbO3 substrate can be clearly observed. This linear correlation can be further extended to the excitation voltage and the acoustic pressure of leaky SAWs in the carrier oil, which has been confirmed numerically and experimentally (partially in Fig. S7A, $R^2 > 0.96$). Based on this assumption, we calculated the nonlinear Reynolds number Re_{nl} based on the method described in Supplementary Note S2, and the predicted curve of Re_{nl} values with respect to increasing acoustic pressures and excitation voltages are shown in Fig. S7B. Generally, the nonlinear Reynolds number Re_{nl} is increased from 0.07 to 4.5 as the excitation voltage is increased from 11.8 Vpp (i.e., pressure threshold at V_T, blue shading in Fig. S7B) to 130 Vpp. The scenario $\mathrm{Re_{nl}}\sim1$ (i.e., 60 Vpp) corresponds to Fig S6 "60 Vpp" where the fluid jets upward (i.e., Jetting mode 1). As $\mathrm{Re_{nl}}$ is increased to higher than a second threshold value between 1.8 - 2.8 (i.e., red shading in Fig. S7B, V_T'), a clear transition between jetting modes is observed. Interestingly, when the air-oil interface is sealed by a plastic slide, we cannot observe distinctive changes in streaming directions for different excitation voltages (Fig. S8). We believe this unexpected new mode (i.e., "100 Vpp", "130 Vpp", Fig. S6) of jetting involves deeper physics entangled with acoustics, fluidics, surface tension, and piezoelectrics and needs further investigation in future studies.

Supplementary Note S4: Influences of the dmIDT geometry on droplet actuation

The influences of IDT geometry on droplet actuation has been preliminarily tested (Fig. S11) using three different designs: a center-expanded IDT, a standard rectangular comb-shaped IDT, and a center-slim IDT (i.e., dmIDT). Generally, although these variations in geometries have negligible influence

on the flow pattern and the manipulation of large droplets (e.g., 430 nL) for either *y*-mode or *x*-mode actuation, the former two IDT designs failed to actuate small droplets/particles under high-excitation signals (i.e., *y*-mode actuation), suggesting that the dmIDT has a larger volume range for droplet manipulation. Fig. S12 demonstrates the trapping of droplets with varied volumes (i.e., 56 – 383 nL) using the slim IDT (i.e., dmIDT) in *y*-mode.

Supplementary Note S5: Contact-free manipulation inside a close-chamber device

A pilot test shows that a 1 mm polystyrene (PS) particle can be trapped by acoustic streaming vortices (i.e., *y*-mode) inside a 2.2 mm-gap sandwiched chip (i.e., with a top substrate sealing the air-oil interface) without contacting any of the substrates (Fig. S13). In this case, the air-oil interface as well as the surface deformation are eliminated. Once the IDT (i.e., red shading) is activated, the ascending fluid jet of FC-40 impinges on the top substrate, recirculates back, and forms two symmetric acoustic streaming vortices inside the chip. However, once the transducer is turned off, the particle will rapidly contact with the top substrate due to buoyancy (i.e., density of water: 1 $g \cdot cm^{-3}$, FC-40: 1.85 $g \cdot cm^{-3}$), leading to potential surface-adsorptions and contaminations on solid surfaces. In the future, we will test different carrier oils with similar density to water (e.g., silicone oil, mineral oil) to slow down the buoyancy effect or sedimentations toward the two substrates during the relayed trap-and-release process of droplet translation. Also, hydrophobic layers (i.e., Teflon) can be coated on the two substrates to minimize potential surface adsorptions like with electro-wetting-based digital microfluidic devices.

Supplementary Note S6: Evaluation of droplet evaporation

The device presented in the manuscript does not have a top cover, which brings benefits such as easy sample addition and collection while leading to challenges for liquid level maintenance and humidity control. This is similar to other existing open substrate mechanisms, including dielectrophoresis (OD

Velev et al. *Nat. Mater. 4,* (2005) 98-102), electrowetting (CJ Kim et al. *Nature, 572,* (2019) 507-510; A Wheeler et al. *Lab Chip, 8,* (2008) 672-677), magnetics (NT Nguyen et al. *Lab Chip, 16,* (2016) 2211-2218), surface tension (Z Wang et al. *Sci. Adv., 3,* (2017) p.eaao3530), thermal flow (YB Gianchandani et al. *J. Microelectromech. Syst. 18,* (2009) 1163-1172), and mechanical forces (PR Onck et al. S*ci. Adv., 5,* (2019) eaaw0914; RH Ras et al. *Adv. Mater., 24,* (2012) 5738-5743), in which evaporation can be a significant issue for liquid handling, especially for droplets at the nanoliter-scale. However, in our device, due to the lower surface tension of fluorinert FC-40 (i.e., 16 dynes·cm^{-1}), the fluorinert oil will spontaneously wet on the water droplets (i.e., 72 dynes·cm^{-1}) as an immiscible coating layer against evaporation, allowing incubation within a short time-span (< 60 min, < 5.8% volume loss) (Fig. S14). Furthermore, under high-amplitude excitations (e.g., 20 Vpp), the droplets will be stably trapped inside the acoustic streaming vortices beneath the oil, which isolates the water droplet from the air and blocks the evaporation. This implies high-amplitude excitation signals (e.g., 20 Vpp) are needed for incubating droplets for relatively long period of time. Additionally, it is possible to devise a simple feedback control system for maintaining air humidity to further minimize the evaporation of water droplets following conventional cell incubators or Poulikakos' study in 2013 (D Poulikakos et al. *Proc. Natl. Acad. Sci. U. S. A. 110,* (2013) 12549-12554), which manipulates aqueous droplets for cell transfection in air using acoustic levitation.

Supplementary Note S7: Droplet manipulation with broken transducers on array

Compared with the electro-wetting on dielectrics (EWOD) technique, since the droplet does not make contact with the solid substrate, our device can withstand issues like surface flaws (e.g., sticky debris) or degradation (e.g., dielectric breakdown), which typically leads to inaccurate actuation. Furthermore, the droplet does not necessarily need to be manipulated by the nearest neighboring units like in EWOD. For example, in the event that an adjacent transducer is damaged or temporarily unavailable, a droplet

can be actuated and gradually trapped by the secondary neighboring transducer, but with much lower speed initially (Fig. S16). This grants our mechanism unique advantages in error-recovery.

Supplementary Note S8: Contactless splitting and merging of droplets

As shown in Fig. S21, a water droplet (i.e., 72 dynes·cm^{-1}) was transported to the center of a transducer and then split by the ascending jets. As the surface tension of the droplet decreases (e.g., ethanol, 22 dynes·cm^{-1}), the voltage required for splitting will be reduced (Fig. S21B and S21C). We will further investigate this function in future studies to stabilize the splitting function. Fig. S15 has demonstrates the feasibility droplet merging process with acoustic streaming vortices. Although there is no surfactant in the oil to maintaining the surface tension barrier, the draining of the oil-film between the two nL-level droplets may take up to several seconds, which suggests an active control for droplet merging (e.g., droplet charging, on-demand sonic/electric de-emulsification) is desired.

Supplementary Note S9: Fluorocarbon oils in microfluidics

Fluorocarbon oils (e.g., HFE-7500 or FC-40, typically containing surfactant) have been widely used in droplet microfluidics for preventing cross-talks between droplets They are inert, oxygen-permeable, and have superior resistivity to diffusion among other filler oils (e.g., mineral oils, silicone oils) commonly used in droplet microfluidics and digital microfluidics platforms, leading to diverse applications such as emulsion PCR, single cell culture, and high-throughput biosynthesis, etc. Conclusively, those well-established applications suggest its good resistance to diffusion and compatibility for routine biochemical reagents in most applications of interest that are not so diffusive. However, fluorine-based chemicals like Telfon, fluoro-surfactants can be dissolved in FC-40 and induce cross-contamination in rare scenarios, implying evaluations on the diffusion-induced cross-contamination are necessary prior to the dispersion of fluorine-based chemicals in fluorocarbon oils.

Supplementary Note S10:

In the beginning of the project, we manually connected and disconnect the wires from the transducer array to the output ports from the amplifier (Fig. S26), which amplifies signals from an arbitrary waveform function generator (AFG 3102C, Tektronix Technology Corporation, PA, USA). The wires were bonded to the gold electrode pads of the transducers using silver epoxy. For modulation of the excitation signals, a computer was used to program the desired signals through the USB connection to the function generator. Recently, we have designed control electronics (Fig. S27A and S27B) to program translation and routing along arbitrary routes (Fig. S27C) on the array shown in Fig. 4F. These supporting electronics includes a chip adaptor, a switch array board, power dividers (i.e., Anzac DS-312), a function generator (i.e., AFG 3102C, Tektronix Technology Corporation, PA, USA), an amplifier (i.e., 25A250A, Amplifier Research Inc., USA), and a mini-computer (i.e., Raspberry Pi 2 Model B). The wires of the transducer array on the lithium niobate substrate were bonded to the chip adaptor using silver epoxy. For the switch array board, the on/off status of each dmIDT is controlled by multiple analog-switches (Analog Device AD5412, MicroChip Inc., USA). Each analog switch on the board is controlled by a configuration bit, and these configuration bits are generated by a micro-computer (Raspberry Pi 2 Model B), and they are stored in the registers (Part No. Texas Instrument SN74AHC595) which are soldered in the center of the IDT-control board.

Supplementary Note S11: Potential echo-based oil-level detection system

In previous experiments, we obtained the desired liquid level by adding a certain volume of carrier oil into a container with known dimensions, which can be roughly validated by measuring the vertical distance between the focal plane of the electrodes and the tracer particles floating on the surface of the oil under a microscope. To maintain a highly consistent liquid level, it is possible to devise an echo-based feedback control system for dynamically monitoring the liquid level in future works. A thin-plate lead zirconate titanate (PZT) transducer (e.g., 0.2 mm thick) will be attached to the IDT array to

serve as a source for generating periodic bulk acoustic waves (BAWs) and as a signal receiver. The pulses of BAWs propagate upward, impinge on the air-oil interface and reflect back, and are finally received by the same PZT transducer (Fig. S28A). By analyzing the time interval between the emitted pulse and received pulse of a designed frequency component (Fig. S28B), the liquid level of the carrier oil can be dynamically monitored. Using this echo-based feedback control system, the oil can be supplied or drained precisely to minimize the variation in oil levels in future systems.

Supplementary Note S12: Selection criteria of design parameters

From the experimental perspective, the acoustic attenuation of the carrier oil is considered to play a dominant role in forming the acoustic streaming vortices and the associated hydrodynamic trapping points. Changing the viscosity of the FC-40 can influence the performance of droplet actuation. By dissolving Teflon into the FC-40 oil, the oil viscosity and the trapping stability can be increased. Yet the tradeoff is that the diffusion of small molecule chemicals will be significantly increased to a level similar to silicone oil and mineral oil, suggesting that in this scenario, additional surfactants or less-diffusive chemicals need to be used to minimize diffusion-induced cross-contamination. We have tested several different carrier fluids like FC-70, FC-40, silicone oil, mineral oil, and water, and found that the FC-40 has acceptable acoustofluidic parameters (e.g., acoustic attenuation, density, viscosity, and surface tension) for efficient droplet actuation, while maintaining remarkable resistance to diffusion of small-molecule chemicals (i.e., Fluorescein, Rhodamine 6G). Though FC-70 has better resistance to diffusion (i.e., 10^{-10} % in co-incubation test), it is much more viscous (i.e., 12 cSt) than FC-40 (i.e., 2.2 cSt) and needs around 2~3-fold higher excitation voltage for droplet actuation, leading to challenges on devising an electronic controller for gating multiplexed, high-voltage radio-frequency signals. Generally, the generation of acoustic streaming vortices and associated hydrodynamic trapping points involves complex interactions between acoustic waves, carrier fluids, and physical boundaries in a 3D space. The key for efficiently creating acoustic streaming vortices is to choose a type of carrier

fluid such that its acoustic attenuation is neither too weak nor too strong. If the acoustic attenuation is too weak (e.g., water, glycerol, or equivalent to a very-thin oil layer), the waves could not transfer their energy to the local carrier fluid and the leaky waves will propagate to neighboring units inside the fluid, causing unexpected acoustic and hydrodynamic interferences between units. If the acoustic attenuation is too strong (e.g., equivalent to a very-thick oil layer), the waves will transfer most of their energy in a short distance near the transducer, which repels droplets floating on the surface of the oil as a strong point-source of flow in the far-field. After multiple tests, we finalized the choice of the carrier fluid (i.e., FC-40), transducer geometry (i.e., center-slim IDT), working frequency (i.e., 49.125 MHz), and the thickness of carrier fluid (i.e., 1.04 mm) to ensure robust actuation of droplets.

Supplementary Note S13: 2D particle image velocimetry (PIV)

In this article, a two-frame, nearest neighbor tracking algorithm is chosen with performance and efficiency both considered. The PIV algorithm developed for this work starts with the detection of individual particles on the video images. Then nearest neighbor searching is utilized to attain the particles' correlation between current frame and the last frame. Background subtraction is first implemented by subtracting each frame image with background, which is calculated by averaging all images. Then the pre-processed images were thresholded and converted into binary mode with the grayscale light intensity in order to reduce the effects of noise in the droplet images. Particles were found and labeled by dividing and recognizing connected domains on the basis of size and shape. Subsequently, the centroid and equivalent radius of each droplet was calculated by circle fitting of droplet's boundary contour. A two-frame nearest neighbor method is implemented specifically for videos in this article. For a series of images $[I_1, I_2, \dots, I_n]$, let I_k be the current frame, and I_{k-1} the last frame. Denote particles in I_k as $[p_{k,1}, p_{k,2}, \dots, p_{k,m_k}]$, then the purpose is to find the correlation between $p_{k,i}$ and $p_{k-1,j}$, where $1 \le i \le m_k$ and $1 \le j \le m_{k-1}$. At the beginning, every particle in the first frame will be given a label. When tracking particle $p_{k,i}$ in frame I_k, the nearest particle in all $p_{k-1,j}$ will be treated as a possible target. If the distance of target and $p_{k,i}$ is smaller than a given threshold L, the target will be given the same label of $p_{k,i}$. If not, the target will be treated as a new particle, with a new label assigned to it. However, there will be some conditions that one particle may

disappear in few frames and arouses again, which is caused by moving away or near from the film plane of camera. An additional strategy was used to solve this problem. When $p_{k,i}$ has no corresponding particle, it will still be treated as potential target in $I_{k+1} \ldots I_{k+t}$, where t represents a limit of number of 'lost' frames. If a particle disappears for more than t frames, it will be treated as a new particle when it arouses again. In this article, particles' size range is about 15-60 pixels in video. L was set to 60 pixels and t was set to 5.

Supplementary Figures.

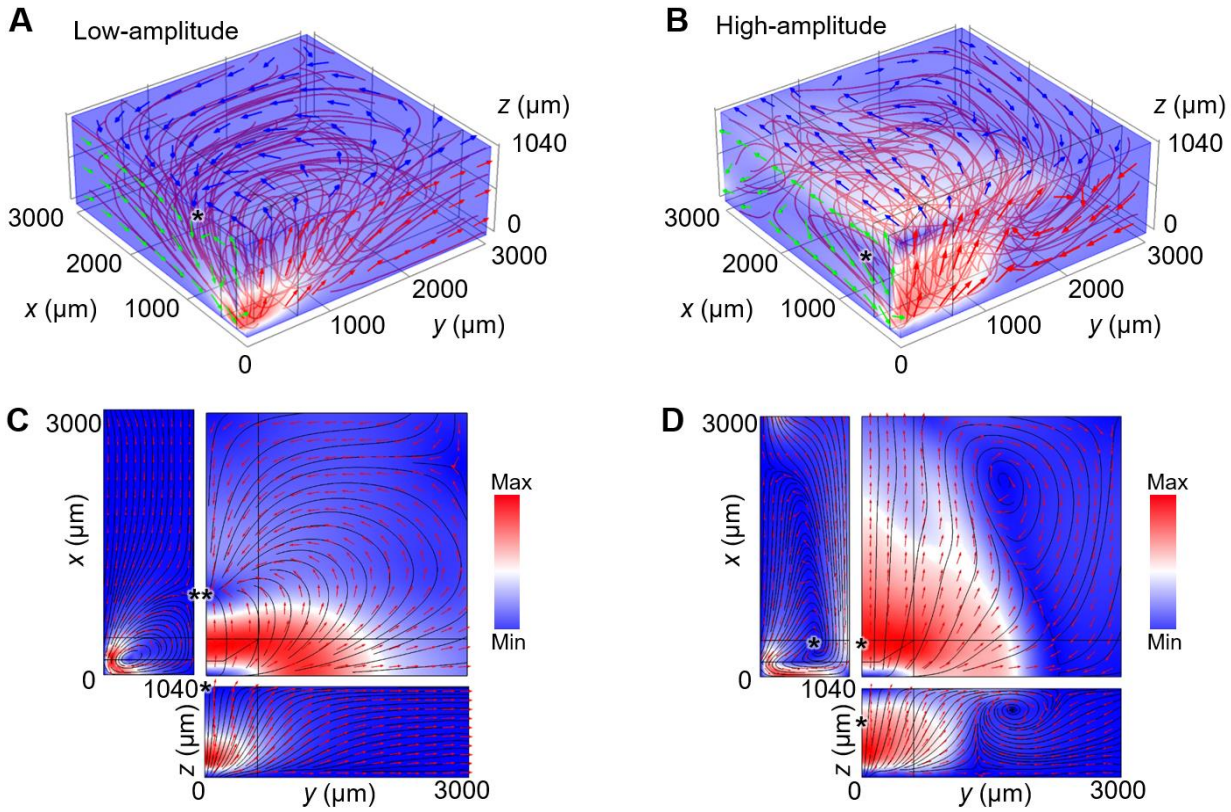

Fig. S1. Simulation results of 3D streamlines over a quarter-transducer excited by (**A**) low-amplitude and (**B**) high-amplitude signals. (**C**) and (**D**) shows the cross-sectional views of the 3D streaming lines when *x*, *y*, and *z* = 0. The hydrodynamic equilibrium positions are indicated by the black asterisks.

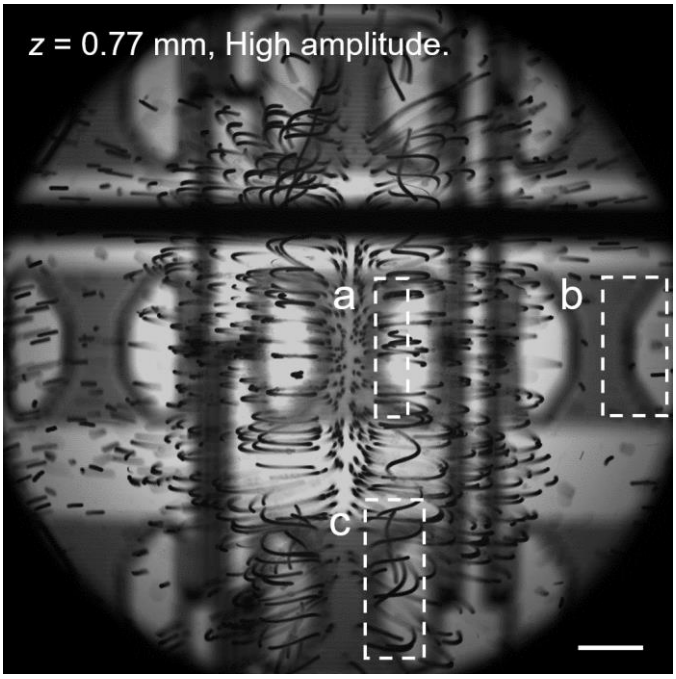

Fig. S2. Microscopic image showing the regions-of-interest (ROIs) selection for the particle image velocimetry (PIV) analysis in Fig. 3. Dashed box (a) indicates the ROI of Fig. 3a (acoustic streaming vortices on oil surface). Dashed box (b) indicates the ROI of Fig. 3b. Dashed box (c) indicates the ROI of Fig. 3c. The excited transducer is located at the center of the figure. Scale bar: 0.5 mm.

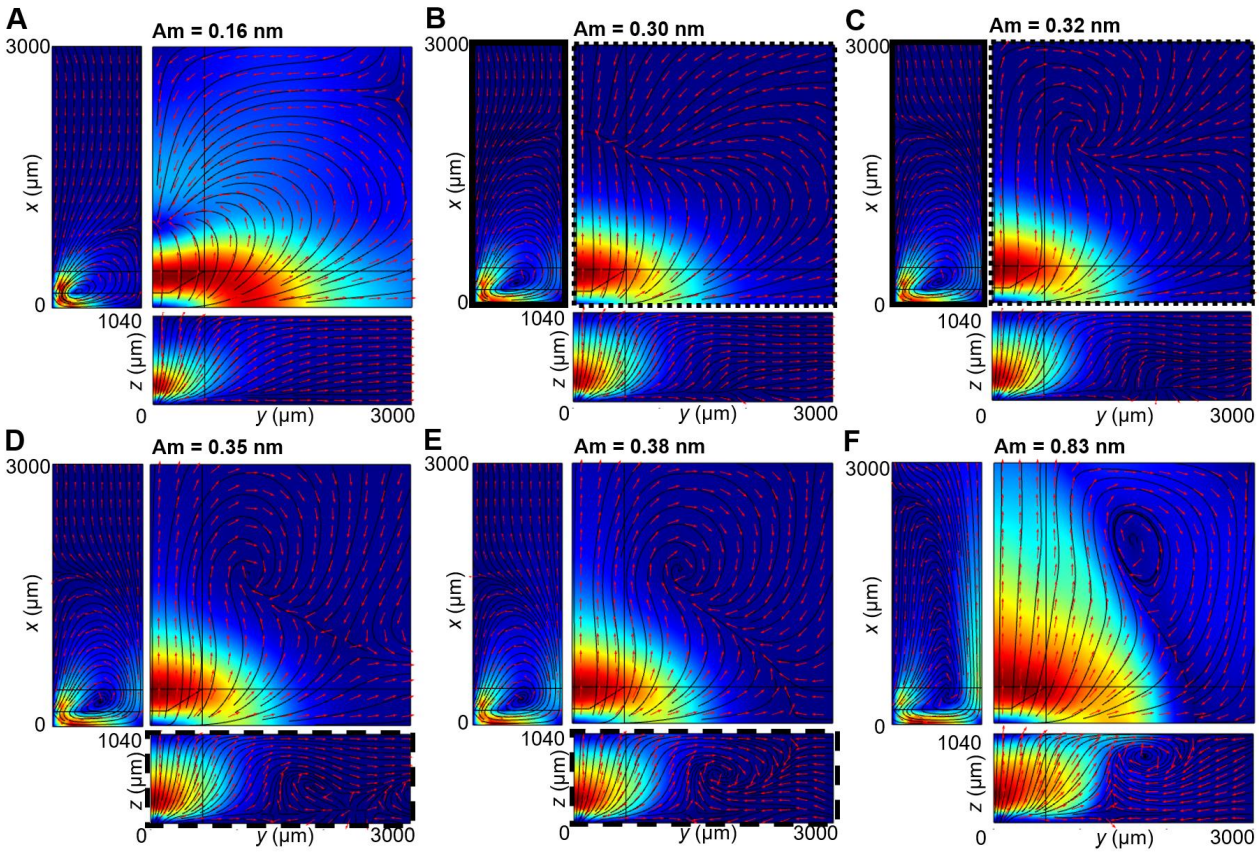

Fig. S3. Cross-sectional views of the simulated 3D streamlines over a quarter-transducer with different vibrational amplitudes (i.e., Am) of SAW on $LiNbO_3$. (**A**) and (**F**) demonstrate the typical acoustic streaming pattern with (**A**) low-amplitude and (**F**) high-amplitude excitation signals, respectively. (**B**) – (**E**) demonstrates the mixed acoustic streaming pattern as the vibrational amplitude increases from 0.30 nm to 0.38 nm and non-linear acoustic gradually dominates. The flowing direction along *x*-axis on the surface of oil (z = 1,040 μm) is reversed when the vibrational amplitude increases from 0.30 nm to 0.32 nm, as indicated by the solid and dotted boxes. The flowing direction along *y*-axis on the surface of the oil (z = 1,040 μm) changed drastically as the vibrational amplitude increases from 0.35 nm to 0.38 nm as indicated by the dashed boxes. The color scale indicates the magnitude of acoustic streaming speed with typical "jet" palette in Matlab.

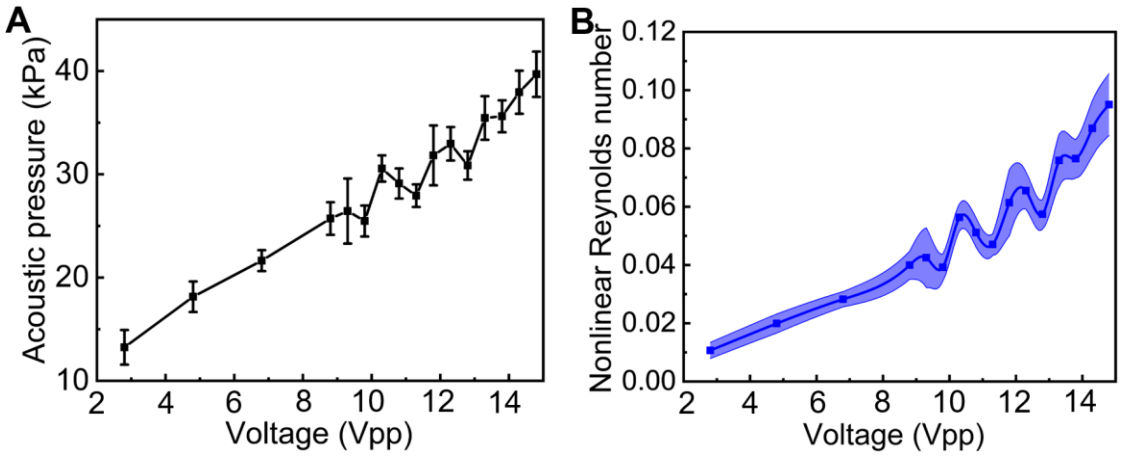

Fig. S4. Acoustic measurement of a dual-mode IDT (dmIDT) with increasing excitation voltages. (**A**) Hydrophone measurement of acoustic pressure in water right above a dmIDT with respect to different excitation voltages on a dmIDT. The pressure measurement is insensitive to the distance between the hydrophone and the excited dmIDT. (**B**) Normalized nonlinear Reynolds number in FC-40 oil with respect to different excitation amplitudes on a dmIDT. The shading area indicates one standard deviation.

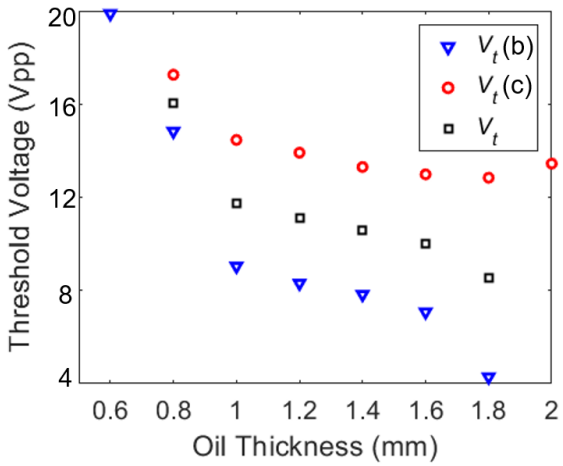

Fig. S5. The relationship between FC-40 oil-thickness and the threshold voltages (V_T (b), V_T (c), and V_T) for a dual-mode IDT (dmIDT) to transit from the *x*-mode acoustic streaming pattern (Fig. 2A) to *y*-mode acoustic streaming (Fig. 2B). The excitation voltage on the dmIDT was increased continuously from 2 Vpp to 20 Vpp in particle tracing experiments to capture the transiting threshold voltages for reversed flows along *y*-axis (V_T (c), red circles) and *x*-axis (V_T (b), blue triangles). Specifically, the threshold voltage V_T (b) (i.e., the blue triangles) is defined as the voltage that the first frame in particle tracing video when reversed flow appears near the flanks of dmIDT (i.e., the region b shown in Fig. S2) along *x*-axis. The threshold voltage V_T (c) (i.e., the red circles) is defined as the voltage that the first frame in particle tracing video when reversed flow appears near the apertures of dmIDT (i.e., the region c shown in Fig. S2) along the *y*-axis (i.e., the direction of SAW propagation). The transiting threshold voltage V_T is the mean value of V_T (b) and V_T (c).

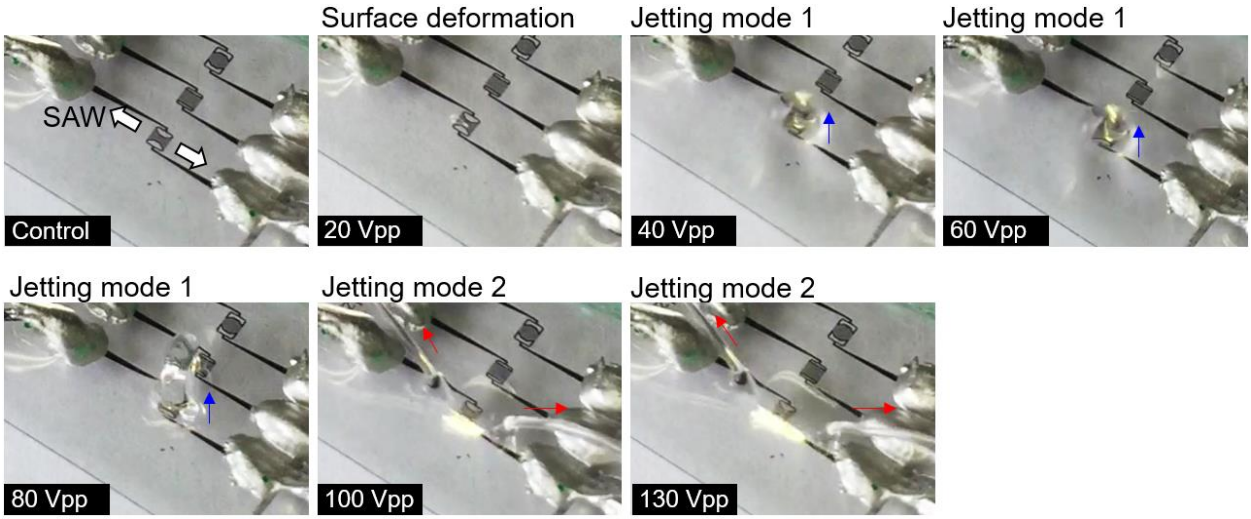

Fig. S6. The fluid response of 1.04 mm thick FC-40 oil under continuous, extremely high excitation voltages. The white arrows indicates the propagation direction of the SAWs from the transducer to be excited. The design of transducer is identical with the transducer in dmIDT presented in the manuscript. The transitions of fluidic responses from “Surface deformation” to “Jetting mode 1”, and from “Jetting mode 1” to “Jetting mode 2” can be clearly observed. The jetting directions of “Jetting mode 1” and “Jetting mode 2” are indicated by the blue and red arrows, respectively.

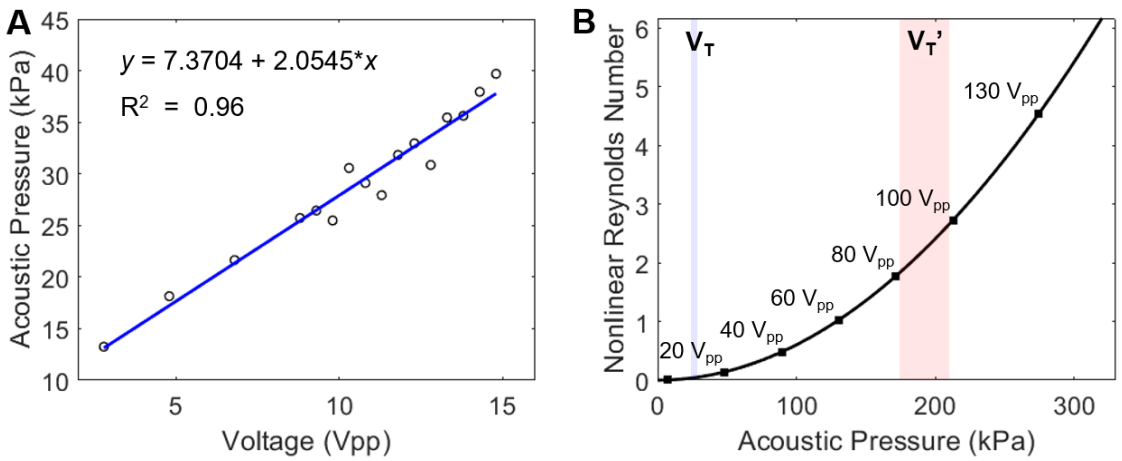

Fig. S7. (**A**) Linear regression of the measured average value of excitation voltages and acoustic pressures. (**B**) The calculated relationship of the nonlinear Reynolds number with respect to acoustic pressure and excitation voltage based on the linear correlation in (**A**). The blue shading indicates the threshold pressure and voltage range of the transition from *x*-mode to *y*-mode streaming (i.e., V_T). The red shading indicates the threshold pressure and voltage range of the transition from mode 1 to mode 2 jetting (i.e., V_T').

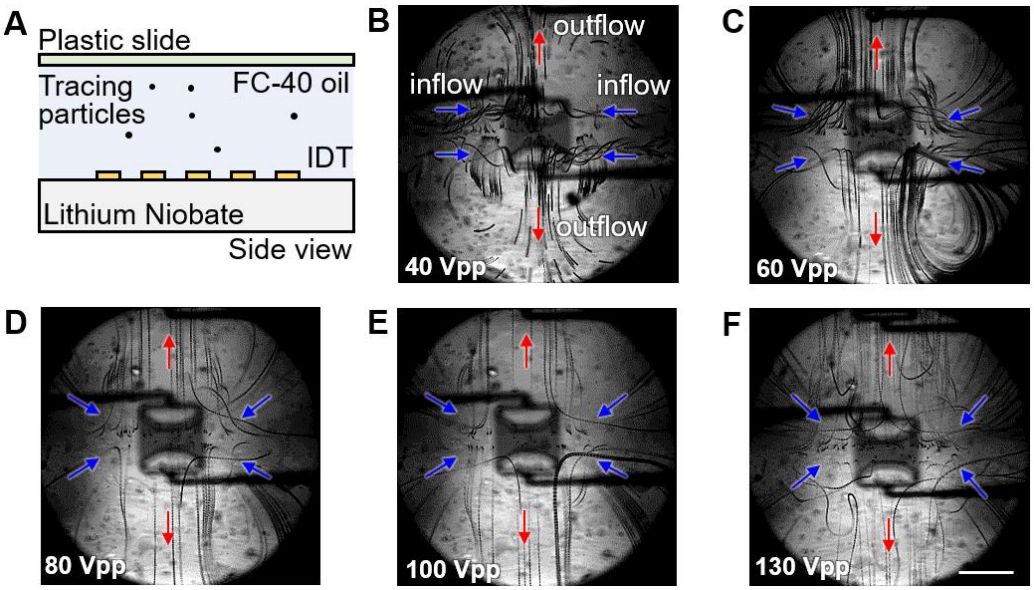

Fig. S8. Characterization of acoustic streaming patterns without surface deformation under extremely high excitation voltages. (**A**) Schematic side view of the experimental device configuration. The air-oil interface is seal with a plastic slides. (**B**) Stacked images showing the trajectories of particle traces under different high excitation voltages. FC-40 oil thickness: 1.04 mm. Bar: 1 mm.

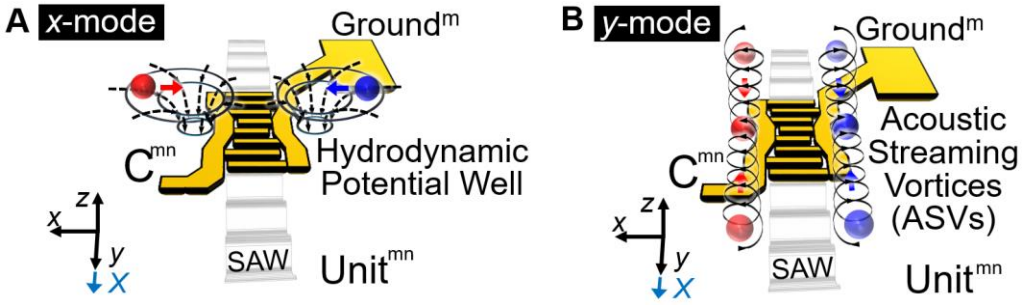

Fig. S9. Schematic of the working principles of a dmIDT. (**A**) With low-excitation amplitude on the dmIDT, the droplet will be translated in ± *x* directions (i.e., *x*-mode). (**B**) With high-excitation amplitude, the droplet will be translated in ± *y* directions inside the extended vortices (i.e., *y*-mode). The blue arrow attached to the coordinates represents the orientation of the *x*-axis of *Y*-128° $LiNbO_3$ substrate. For an array contains $m \times n$ transducers, The label "Unit^{mn}" represents the unit in the mth row and the nth column in an array. "Ground^{m}" represents the ground wire of the mth row. "C^{mn}" represents the controlling signal wire of Unit^{mn}. The red and blue spheres represents the floating droplets on the fluorinert oil.

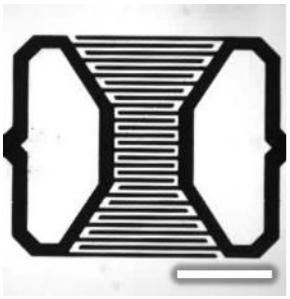

Fig. S10. Microscopic image of a dmIDT. The size of the transducer is 0.87 mm × 1.18 mm. Scale bar: 0.5 mm.

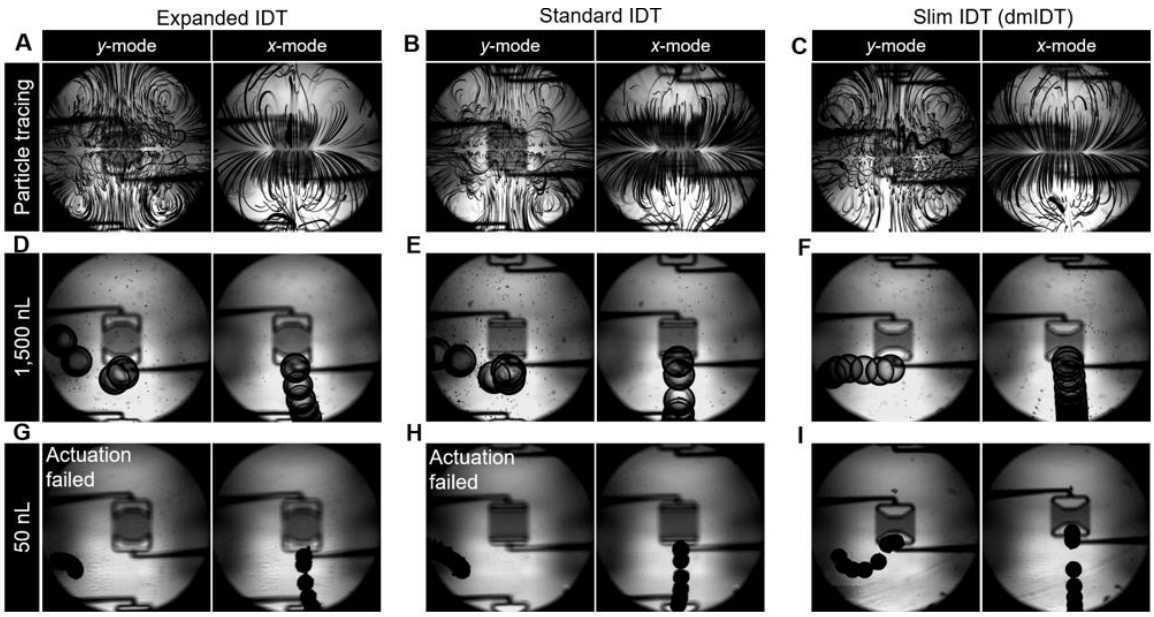

Fig. S11. Characterization of dmIDTs with three typical geometries. (**A**)-(**C**) Stacked image of particle tracing of the IDTs with three different geometries under high- (i.e., *y*-mode) and low-amplitude (i.e., *x*-mode) excitation signals. (**D**)-(**F**) Stacked image of large droplet actuation using IDTs with three different geometries under high- (i.e., *y*-mode) and low-amplitude (i.e., *x*-mode) excitation signals. (**G**)-(**I**) Stacked image of small particle (i.e., 475 μm) actuation using IDTs with three different geometries under high- (i.e., *y*-mode) and low-amplitude (i.e., *x*-mode) excitation signals. Note that a polystyrene particle are used to test the small droplet actuation scenario in place of aqueous of droplet due to the inconsistency of droplet dispensing at the nanoliter-level. (**A**)(**D**)(**G**) IDT with expansion geometry in the center. (**B**)(**E**)(**H**) IDT with standard rectangular comb shape. (**C**)(**F**)(**I**) IDT with slim geometry in the center (i.e., dmIDT).

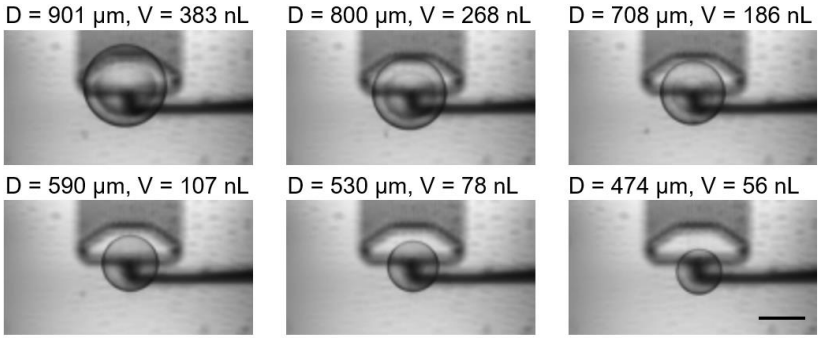

Fig. S12. Contactless trapping of droplets with varied volumes (i.e., 56 – 383 nL) with acoustic streaming vortices using *y*-mode dmIDT. D: droplet diameter. V: droplet volume. Bar: 0.5 mm.

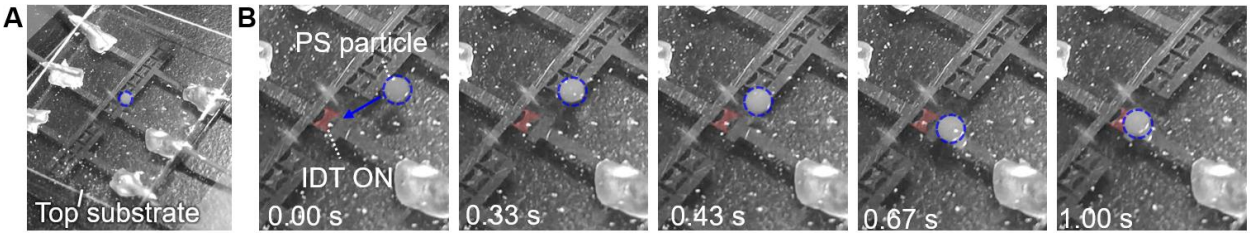

Fig. S13. Contactless droplet actuation in a closed fluid system without an air-oil interface. (**A**) A sandwiched chip with a plastic slide to seal the air-oil interface. (**B**) Polystyrene particle (1 mm) trapping inside a sandwiched chip *via* acoustic streaming vortices.

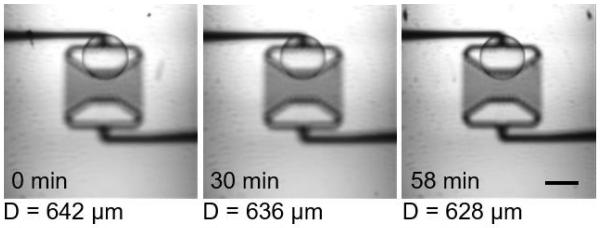

Fig. S14. Time-elapsed images of droplet evaporation while being trapped by acoustic streaming vortices. Excitation amplitude: 20 Vpp. D: droplet diameter. V: droplet volume. Bar: 0.5 mm. The surface tension of the oil is low; therefore, the water droplet can be approximated as a spherical object to calculate the volume.

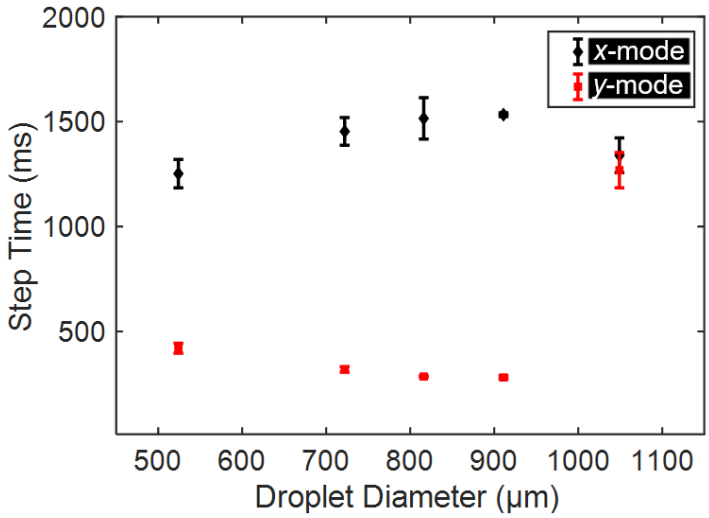

Fig. S15. The relationship between droplet volume and step time (i.e., for moving a droplet for 1.8 mm) in *x*- and *y*-mode using dmIDT.

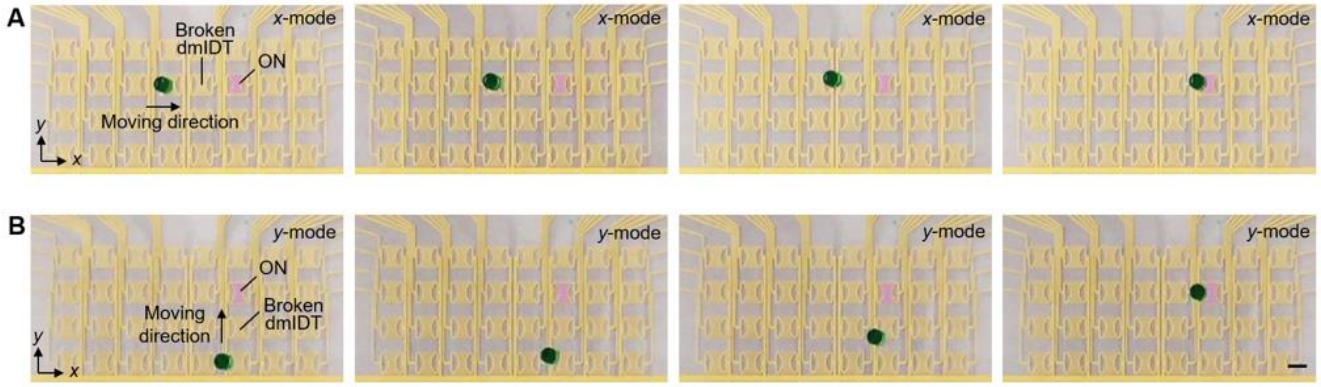

Fig. S16. Contactless droplet actuation using the secondary neighboring transducer using (**A**) low-amplitude (i.e., *x*-mode) and (**B**) high-amplitude (i.e., *y*-mode) excitation signals. The purple shadings indicate the positions of the excited transducers. Bar: 1 mm.

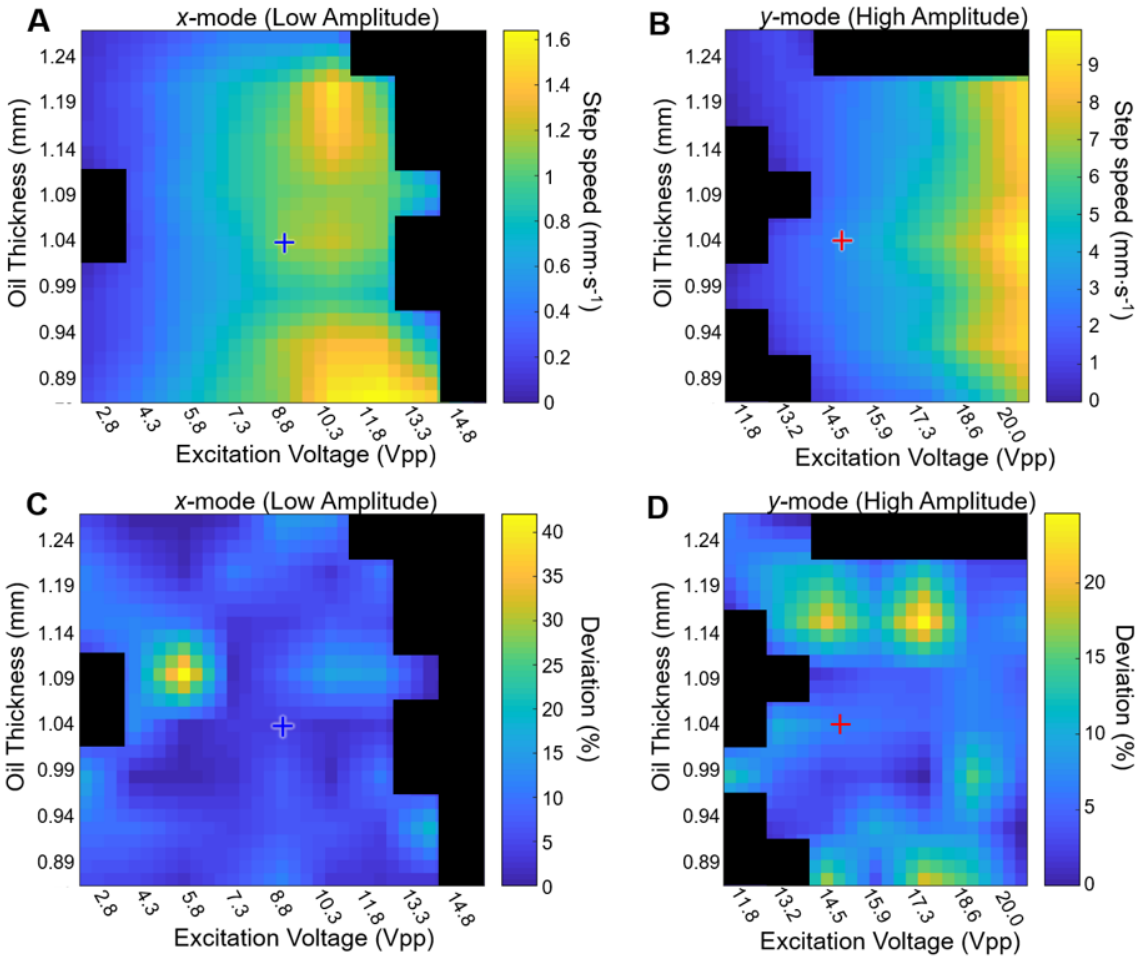

Fig. S17. The influence of variations in the thickness of the oil-layer thickness and the excitation voltage on the average moving speed using (**A**) *x*-mode and (**B**) *y*-mode acoustic streaming for actuating a 0.95-mm-diameter polystyrene particle a distance of 1.9 mm. The deviations in speed (in percentage) for *x*-mode and *y*-mode dmIDTs are shown in (**C**) and (**D**), respectively. The heatmaps were smoothed using linear interpolation and the values of step time are scaled to the parula colormap. The black shades indicate the parametric space that the particle cannot be robustly actuated. The blue and red crosses indicate the choices of parameters for *x*-mode and *y*-mode, respectively.

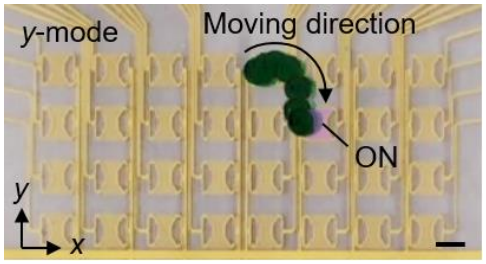

Fig. S18. Stacked image of the re-stabilization process of a droplet swayed from the anticipated initial position using high-amplitude excitation signals (i.e., *y*-mode). Bar: 1 mm.

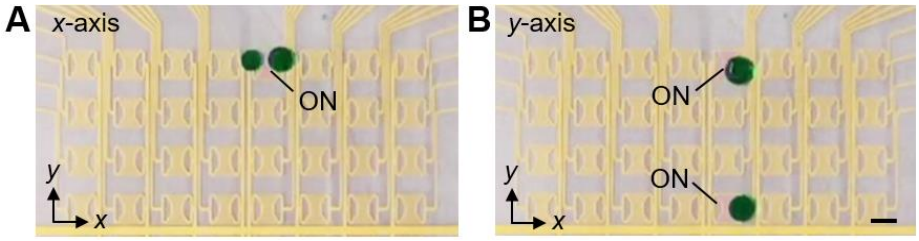

Fig. S19. Simultaneous, contactless droplet trapping using high-amplitude excitation signals (i.e., *y*-mode) with minimal droplet separation distance along (**A**) *x*-axis and (**B**) *y*-axis. Bar: 1mm.

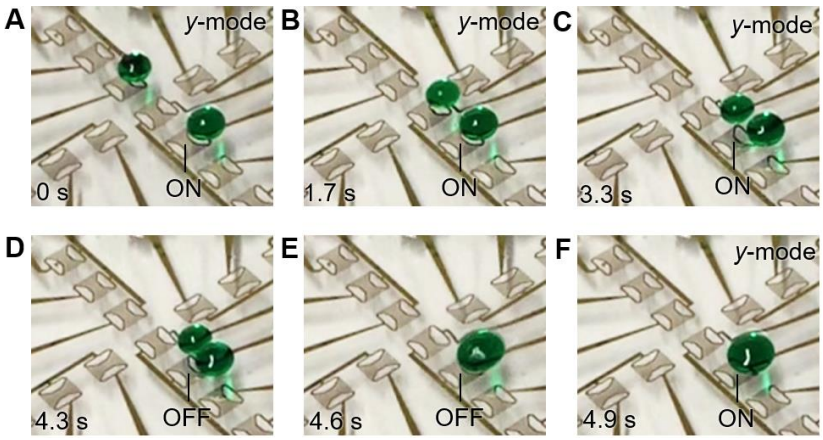

Fig. S20. Droplet merging process *via* acoustic streaming vortices. The droplets were firstly brought close by the acoustic streaming, then make contact with each other due to the Cheerios effect, and finally merge together. The dimensions of the transducer are 2.2 mm × 3.5 mm and the working frequency is 23.9 MHz. Oil thickness: 1.6 mm.

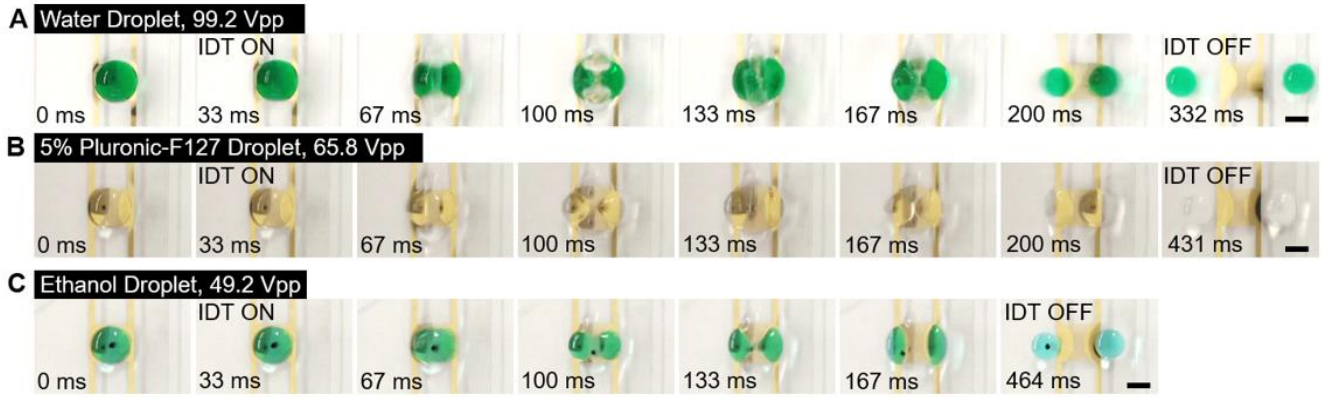

Fig. S21. Contactless splitting of droplets with different surface tensions. (**A**) Splitting of a 50 µL water droplet. (**B**) Splitting of a 50 µL water droplet containing 5 % Pluronic F127 surfactant. (**C**) Splitting of a 30 µL ethanol droplet. Transducer dimension: 2.240 mm × 3.124 mm. Working frequency: 23.9 MHz. Oil layer thickness: 2.5 mm. Scale bars: 2 mm.

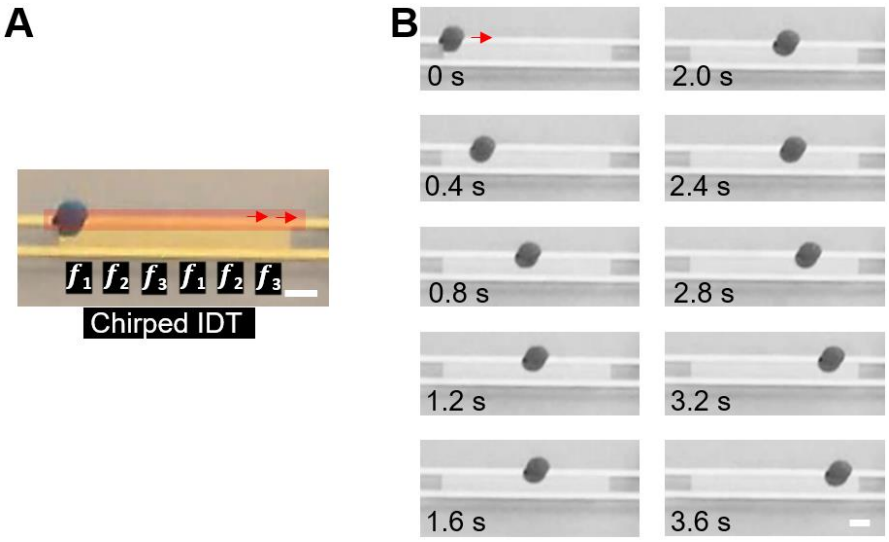

Fig. S22. Contactless, unidirectional translation of a solid particle *via* the acoustic-streaming vortices generated by the chirped IDT. (**A**) Device picture of chirped IDT. (**B**) Time-elapsed image of the particle being translated from left to right. A periodical frequency modulated signal is applied to the chirped IDT device. Scale bars: 1 mm.

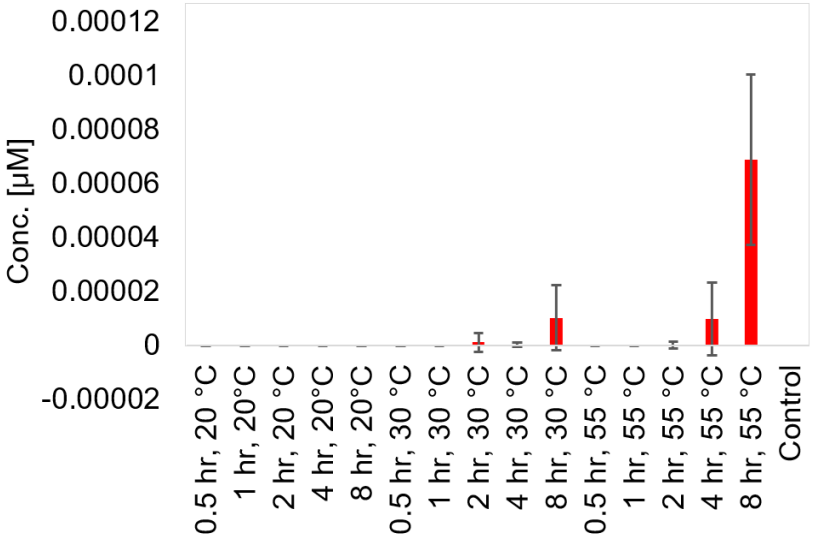

Fig. S23. Characterization of diffusion of Rhodomine 6G in fluorinert FC-40 oil. Rhodamine 6G are dissolved in pure water to a final concentration of 100 µM. 500 µL of dye solution was dispensed with 700 µL of fluorinert FC-40 oil into 1.5 ml tubes for incubation. The incubation tests had different elapsed times (0.5 hr, 1 hr, 2 hr, 4 hr, and 8 hr) and environment temperatures (20 °C, 30 °C, and 55 °C). After incubation, triplicate 200 µL of FC-40 oil were carefully transferred from each tube from bottom to top to a 96-well plate for fluorescence measurement by a plate reader. The concentrations are derived from a standard concentration-fluorescence curve.

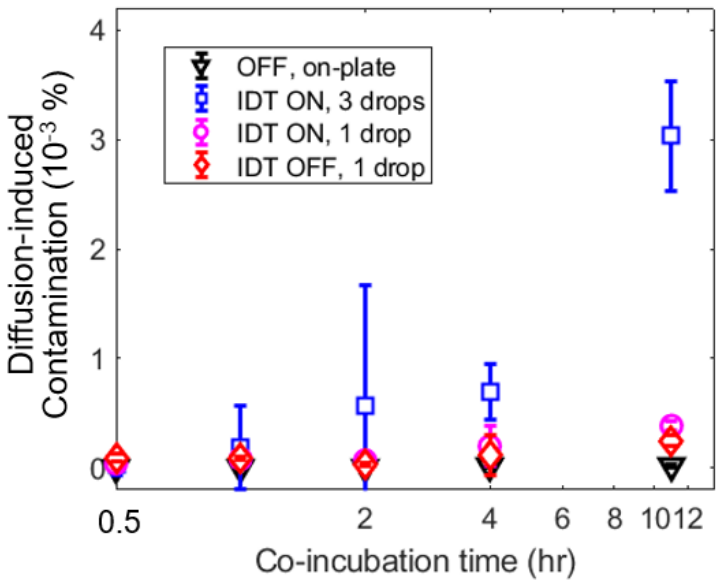

Fig. S24. Characterization of the diffusion of Rhodamine 6G to a water droplet during on-chip co-incubation. The experiments are tested with two attached 2.5 μL droplets (i.e., one droplet contains water only, the other one contains 100 μM Rhodamine 6G) near the two apertures of a *y*-mode transducer with a separation distance of 4 mm ('IDT ON, 1 drop', purple circles). Another water droplet was placed next to the first water droplet with a separation distance of 4 mm ('IDT OFF, 1 drop', red diamonds) as control, in which scenario the influence of acoustic streaming generated by the *y*-mode transducer was minimized. After 0.5 hr, 1 hr, 2 hr, 4 hr, and 11 hr co-incubation, the droplets are transferred to a 96-well plate for fluorescence measurements. The diffusion of 3 dyed droplets to 3 water droplets was characterized ('IDT ON, 3 drops', blue squares). Additionally, the diffusion between a 50 μL water droplet and a 50 μL Rhodamine 6G droplet is indicated by 'OFF, on-plate', black triangles. The detailed experimental procedures is described in the Methods section.

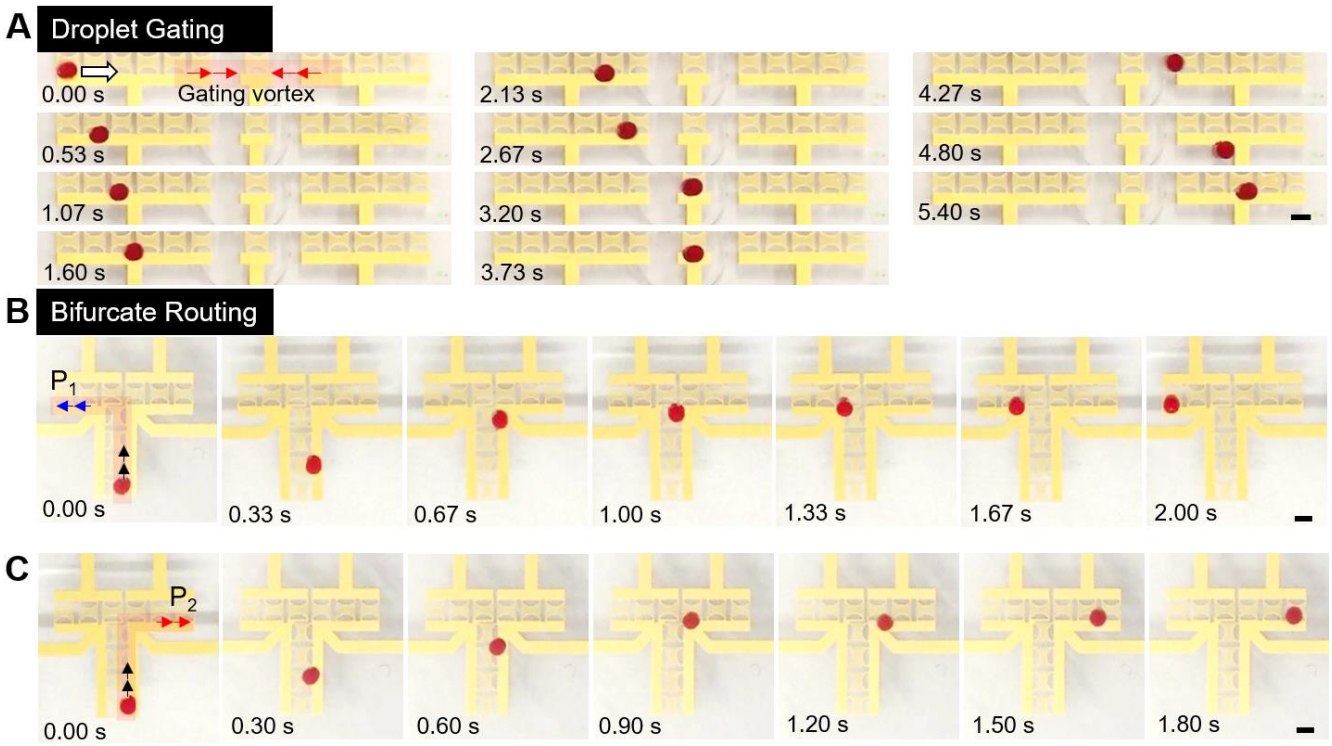

Fig. S25. (**A**) Contactless gating and (**B**) (**C**) bifurcated routing (i.e., sorting) of a 0.91 mm polystyrene particle at maximum speed. On the bifurcated routing device, the particle can be either transported to port P_1 (**B**) or port P_2 (**C**). The red shaded area indicates the virtual fluidic channel formed by interconnected acoustic streaming vortices. Bars: 1 mm.

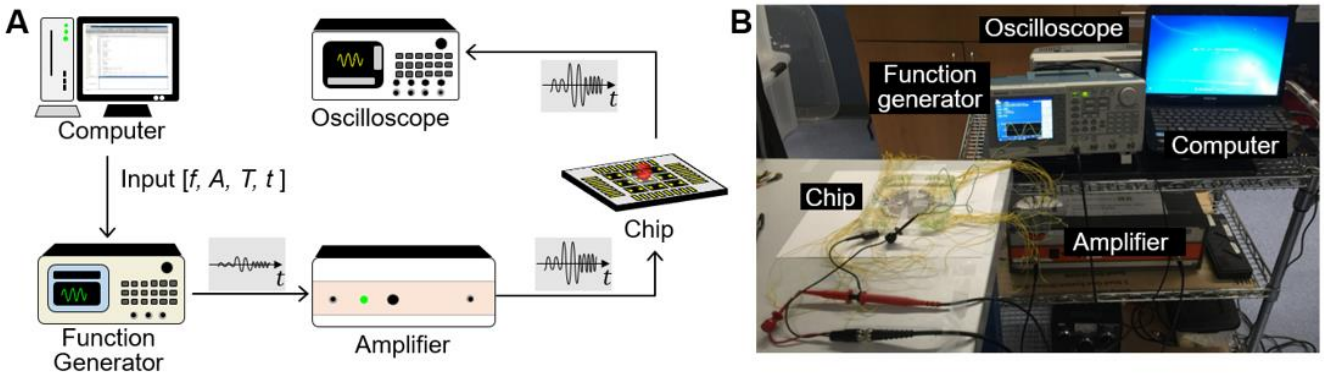

Fig. S26. (**A**) Schematic overview of the experimental set up. The computer sends input parameters including frequency (*f*), amplitude (*A*), duration (*T*), and excitation time-point (*t*) to the function generator. The function generator synthetizes the desired multi-tonal signals, which are then amplified by the amplifier to power the transducers on chip. The oscilloscope attach to the excited transducer to monitor the electric performance of the transducer. (**B**)A photo showing the arrangement of the equipment. The yellow wires were bonded to the chip using silver epoxy and are connected to the output port and oscilloscope.

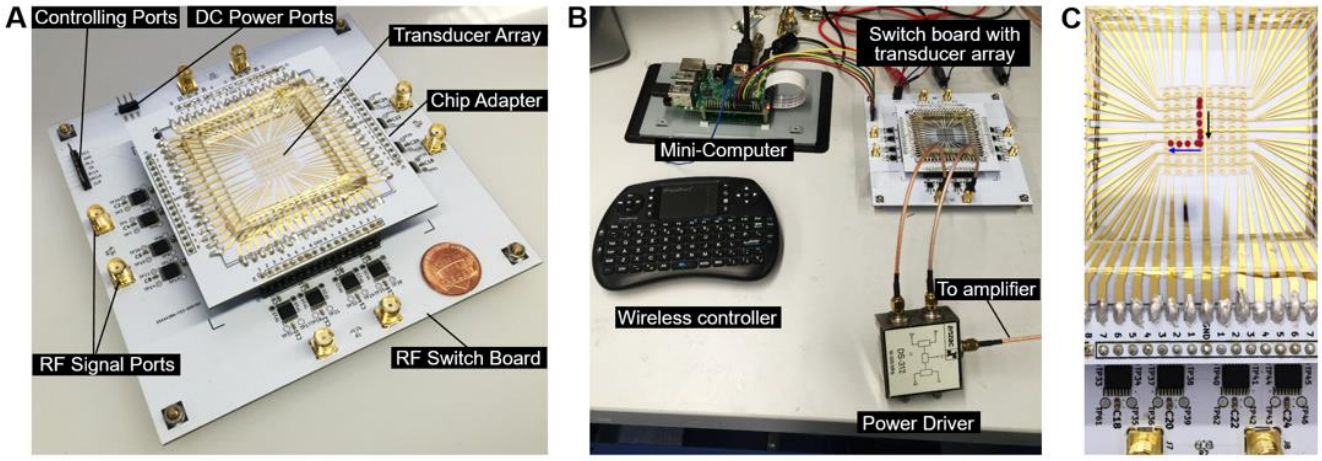

Fig. S27. (**A**) Integration of surface acoustic wave transducer array with radio-frequency (RF) electronics. (**B**) Overview of the system setup with RF signal switching board. (**C**) Contactless routing of a 0.91 mm polystyrene particle. The black arrow indicates the direction of *x*-mode actuation (i.e., low amplitude excitation), and the blue arrow indicates the direction of *y*-mode actuation (i.e., high-amplitude excitation).

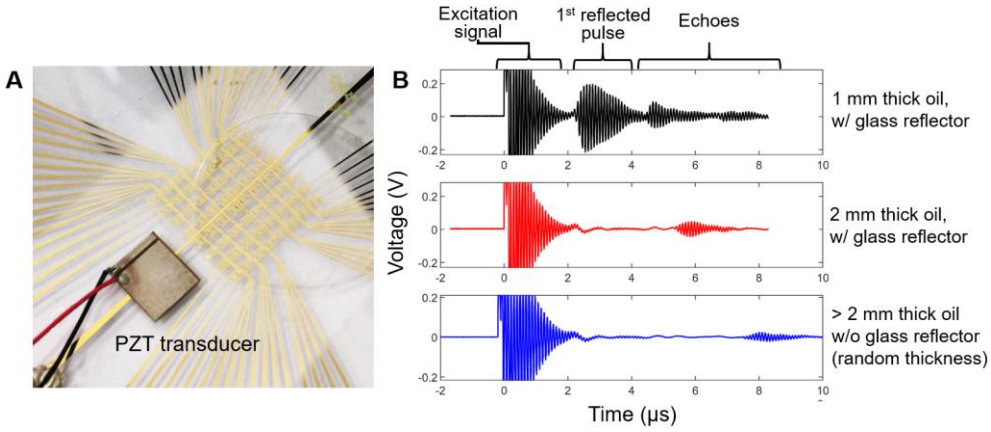

Fig. S28. Acoustic sensing for monitoring oil level. (**A**) Experimental setup. (**B**) Signals received by the PZT transducer plate immersed in FC-40.

Supplementary Movies.

Movie S1. Particle tracking results with low-amplitude excitation signal (*x*-mode, z = 1.04 mm). This video was captured at 500 fps and replayed at 30 fps.

Movie S2. Particle tracking results with high-amplitude excitation signal (*y*-mode, z = 0.77 mm). This video was captured at 500 fps and replayed at 30 fps.

Movie S3. Droplet trapping with high-amplitude excitation signal (*y*-mode). Flow-tracing particles are employed to demonstrate the streaming pattern. This video was captured at 500 fps and replayed at 30 fps.

Movie S4. Particle tracking of the internal streaming inside a droplet trapped by *y*-mode transducers. This video was captured at 250 fps and replayed at 30 fps.

Movie S5. Parallel droplet actuation with miniaturized transducer array. This video is in real-time.

Movie S6. Unidirectional droplet gating using frequency-modulated signals. This video was captured at 500 fps and replayed at 30 fps.

Movie S7. Repeated droplet translation with a step time of 0.5 s. This video is in real-time.

Movie S8. Contactless droplet rotation without external control. This video is in real-time.

Movie S9. Contactless droplet gating. This video is in real-time.

Movie S10. Contactless bifurcated droplet routing with two sets of frequency modulated signals. This video is in real-time.

REFERENCES AND NOTES

1. J. Bardeen, W. H. Brattain, The transistor, a semi-conductor triode. *Phys. Rev.* **74**, 230–231 (1948).

2. G. Katsikis, J. S. Cybulski, M. Prakash, Synchronous universal droplet logic and control. *Nat. Phys.* **11**, 588–596 (2015).

3. J. C. Baret, O. J. Miller, V. Taly, M. Ryckelynck, A. El-Harrak, L. Frenz, C. Rick, M. L. Samuels, J. B. Hutchison, J. J. Agresti, D. R. Link, D. A. Weitz, A. D. Griffiths, Fluorescence-activated droplet sorting (FADS): Efficient microfluidic cell sorting based on enzymatic activity. *Lab Chip* **9**, 1850–1858 (2009).

4. O. D. Velev, B. G. Prevo, K. H. Bhatt, On-chip manipulation of free droplets. *Nature* **426**, 515–516 (2003).

5. M. G. Pollack, R. B. Fair, A. D. Shenderov, Electrowetting-based actuation of liquid droplets for microfluidic applications. *Appl. Phys. Lett.* **77**, 1725–1726 (2000).

6. A. R. Wheeler, Chemistry. Putting electrowetting to work. *Science* **322**, 539–540 (2008).

7. J. Li, N. S. Ha, T. Liu, R. M. van Dam, C.-J. `CJ' Kim, Ionic-surfactant-mediated electro-dewetting for digital microfluidics. *Nature* **572**, 507–510 (2019).

8. A. Ozcelik, J. Rufo, F. Guo, Y. Gu, P. Li, J. Lata, T. J. Huang, Acoustic tweezers for the life sciences. *Nat. Methods*, **15**, 1021–1028 (2018).

9. E. H. Trinh, Compact acoustic levitation device for studies in fluid dynamics and material science in the laboratory and microgravity. *Rev. Sci. Instrum.* **56**, 2059–2065 (1985).

10. A. Marzo, B. W. Drinkwater, Holographic acoustic tweezers. *Proc. Natl. Acad. Sci. U.S.A.* **116**, 84–89 (2019).

11. A. Wixforth, C. Gauer, J. Scriba, M. Wassermeier, R. Kirchner, Flat fluidics: A new route toward programmable biochips. *Microfluid. BioMEMS Med. Microsyst.* **4982**, 235 (2003).

12. S. Collignon, J. Friend, L. Yeo, Planar microfluidic drop splitting and merging. *Lab Chip* **15**, 1942–1951 (2015).

13. P. Li, Z. Ma, Y. Zhou, D. J. Collins, Z. Wang, Y. Ai, Detachable acoustophoretic system for fluorescence-activated sorting at the single-droplet level. *Anal. Chem.* **91**, 9970–9977 (2019).

14. D. J. Collins, T. Alan, K. Helmerson, A. Neild, Surface acoustic waves for on-demand production of picoliter droplets and particle encapsulation. *Lab Chip* **13**, 3225–3231 (2013).

15. J. Reboud, Y. Bourquin, R. Wilson, G. S. Pall, M. Jiwaji, A. R. Pitt, A. Graham, A. P. Waters, J. M. Cooper, Shaping acoustic fields as a toolset for microfluidic manipulations in diagnostic technologies. *Proc. Natl. Acad. Sci. U.S.A.* **109**, 15162–15167 (2012).

16. D. Foresti, M. Nabavi, M. Klingauf, A. Ferrari, D. Poulikakos, Acoustophoretic contactless transport and handling of matter in air. *Proc. Natl. Acad. Sci. U.S.A.* **110**, 12549–12554 (2013).

17. C. N. Baroud, M. R. de Saint Vincent, J.-P. Delville, An optical toolbox for total control of droplet microfluidics. *Lab Chip* **7**, 1029–1033 (2007).

18. C. Yang, G. Li, A novel magnet-actuated droplet manipulation platform using a floating ferrofluid film. *Sci. Rep.* **7**, 15705 (2017).

19. E. De Jong, Y. Wang, J. M. J. Den Toonder, P. R. Onck, Climbing droplets driven by mechanowetting on transverse waves. *Sci. Adv.* **5**, eaaw0914 (2019).

20. T. Thorsen, R. W. Roberts, F. H. Arnold, S. R. Quake, Dynamic pattern formation in a vesicle-generating microfluidic device. *Phys. Rev. Lett.* **86**, 4163–4166 (2001).

21. S.-Y. Teh, R. Lin, L.-H. Hung, A. P. Lee, Droplet microfluidics. *Lab Chip* **8**, 198–220 (2008).

22. J. Li, Q. H. Qin, A. Shah, R. H. A. Ras, X. Tian, V. Jokinen, Oil droplet self-transportation on oleophobic surfaces. *Sci. Adv.* **2**, e1600148 (2016).

23. J. Li, X. Zhou, J. Li, L. Che, J. Yao, G. McHale, M. K. Chaudhury, Z. Wang, Topological liquid diode. *Sci. Adv.* **3**, eaao3530 (2017).

24. W. Lei, G. Hou, M. Liu, Q. Rong, Y. Xu, Y. Tian, L. Jiang, High-speed transport of liquid droplets in magnetic tubular microactuators. *Sci. Adv.* **4**, eaau8767 (2018).

25. A. M. Klein, L. Mazutis, I. Akartuna, N. Tallapragada, A. Veres, V. Li, L. Peshkin, D. A. Weitz, M. W. Kirschner, Droplet barcoding for single-cell transcriptomics applied to embryonic stem cells. *Cell* **161**, 1187–1201 (2015).

26. R. H. Cole, S.-Y. Tang, C. A. Siltanen, P. Shahi, J. Q. Zhang, S. Poust, Z. J. Gartner, A. R. Abate, Printed droplet microfluidics for on demand dispensing of picoliter droplets and cells. *Proc. Natl. Acad. Sci. U.S.A.* **114**, 8728–8733 (2017).

27. M. Prakash, N. Gershenfeld, Microfluidic bubble logic. *Science* **315**, 832–835 (2007).

28. P. N. Duncan, T. V. Nguyen, E. E. Hui, Pneumatic oscillator circuits for timing and control of integrated microfluidics. *Proc. Natl. Acad. Sci. U.S.A.* **110**, 18104–18109 (2013).

29. H. Mertaniemi, R. Forchheimer, O. Ikkala, R. H. A. Ras, Rebounding droplet-droplet collisions on superhydrophobic surfaces: From the phenomenon to droplet logic. *Adv. Mater.* **24**, 5738–5743 (2012).

30. T. Thorsen, S. J. Maerkl, S. R. Quake, Microfluidic large-scale integration. *Science* **298**, 580–584 (2002).

31. V. N. Luk, G. C. H. Mo, A. R. Wheeler, Pluronic additives: A solution to sticky problems in digital microfluidics. *Langmuir* **24**, 6382–6389 (2008).

32. P. Gruner, B. Riechers, B. Semin, J. Lim, A. Johnston, K. Short, J.-C. Baret, Controlling molecular transport in minimal emulsions. *Nat. Commun.* **7**, 10392 (2016).

33. A. S. Basu, Y. B. Gianchandani, A 128-pixel digitally-programmable microfluidic platform for non-contact droplet actuation using marangoni flows, in *TRANSDUCERS 2007—2007 International Solid-State Sensors, Actuators and Microsystems Conference* (IEEE, 2007), pp. 771–774.

34. X. Y. Du, M. E. Swanwick, Y. Q. Fu, J. K. Luo, A. J. Flewitt, D. S. Lee, S. Maeng, W. I. Milne, Surface acoustic wave induced streaming and pumping in 128° Y-cut $LiNbO_3$ for microfluidic applications. *J. Micromech. Microeng.* **19**, 035016 (2009).

35. M. Alghane, B. X. Chen, Y. Q. Fu, Y. Li, J. K. Luo, A. J. Walton, Experimental and numerical investigation of acoustic streaming excited by using a surface acoustic wave device on a 128° YX-$LiNbO_3$ substrate. *J. Micromech. Microeng.* **21**, 015005 (2011).

36. A. Karimi, S. Yazdi, A. M. Ardekani, Hydrodynamic mechanisms of cell and particle trapping in microfluidics. *Biomicrofluidics* **7**, 21501 (2013).

37. S. Boluriaan, P. J. Morris, Acoustic streaming: From Rayleigh to today. *Int. J. Aeroacoustics* **2**, 255–292 (2003).

38. M. K. Aktas, B. Farouk, Numerical simulation of acoustic streaming generated by finite-amplitude resonant oscillations in an enclosure. *J. Acoust. Soc. Am.* **116**, 2822–2831 (2004).

39. L. Menguy, J. Gilbert, Non-linear acoustic streaming accompanying a plane stationary wave in a guide. *Acust.* **86**, 249–259 (2000).

40. G. D. West, Circulations occurring in acoustic phenomena. *Proc. Phys. Soc. Sect. B* **64**, 483–487 (1951).

41. U. Ingård, S. Labate, Acoustic circulation effects and the nonlinear impedance of orifices. *J. Acoust. Soc. Am.* **22**, 211–218 (1950).